ANNUAL REVIEWS

Annual Review of Earth and Planetary Sciences

Back-Projection Imaging of Earthquakes

Eric Kiser[1] and Miaki Ishii[2]

[1]Department of Geosciences, University of Arizona, Tucson, Arizona 85721; email: ekiser@email.arizona.edu

[2]Department of Earth and Planetary Sciences, Harvard University, Cambridge, Massachusetts 02138; email: ishii@eps.harvard.edu

Annu. Rev. Earth Planet. Sci. 2017. 45:271–99

First published as a Review in Advance on May 31, 2017

The *Annual Review of Earth and Planetary Sciences* is online at earth.annualreviews.org

https://doi.org/10.1146/annurev-earth-063016-015801

Keywords

back-projection, rupture properties, megathrust earthquakes, intermediate-depth earthquakes, earthquake detection, seismic array

Abstract

Back-projection analysis of earthquakes is a type of array processing that images the source of seismic waves coherently recorded at stations throughout the seismic network. The method was developed following the magnitude 9.2 Sumatra-Andaman earthquake in 2004. Although properties of earthquakes have been investigated using array data prior to the introduction of the back-projection method, this technique differs from other approaches because it makes limited assumptions and allows detailed and complex rupture propagation to be examined. These advantages have led several researchers to apply the method to many of the largest earthquakes to occur this century. The method has also been effective for the detection of smaller events. A critical component of the success of back-projection has been the development of large-scale, dense seismic arrays. Further improvements and future applications of the method will depend greatly on the continued maintenance and development of these networks.

INTRODUCTION

Identification and characterization of earthquakes around the world are some of the most important aspects of seismology. Near-real-time monitoring of seismicity is performed both at the global level [e.g., National Earthquake Information Center, US Geological Survey (USGS); **https://earthquake.usgs.gov**) and at the regional scale [e.g., Japan Meteorological Agency (JMA); **http://www.jma.go.jp/jma/index.html**], and information such as earthquake location and size is used to guide rapid earthquake response efforts or to estimate the potential for devastating tsunamis (e.g., Hayes et al. 2011). Of particular concern are large earthquakes, such as the magnitude 9.2 Sumatra-Andaman earthquake from December 26, 2004, that can result in widespread destruction and transoceanic tsunamis. For these giant events, the displacement on the fault occurs over a large area with significant implications for the extent of damage. For example, the 2004 Sumatra-Andaman earthquake began offshore of the northern Sumatra island and propagated along the trench toward the north end of the Andaman archipelago, about 1,200 km from where it started (**Figure 1**). This earthquake generated large tsunami waves that devastated, among other

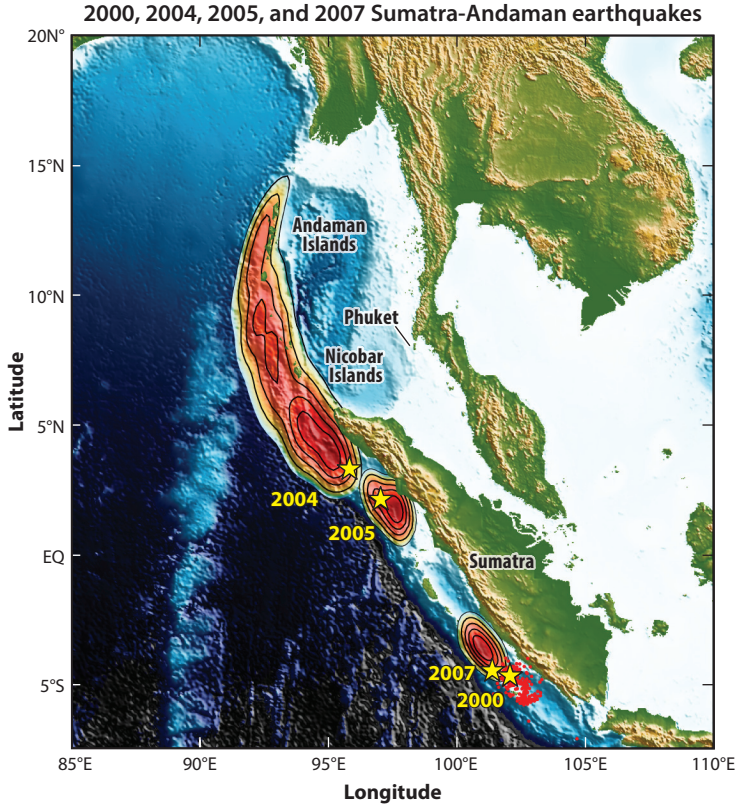

Figure 1

Sumatran earthquake sequence. The rupture areas of the 2004 Mw 9.2, 2005 Mw 8.6, and 2007 Mw 8.5 great earthquakes along the Sumatran subduction zone are shown in color with contours from back-projection analyses. The red dots indicate aftershock activity following the 2000 magnitude 7.9 event. The yellow stars indicate the respective epicentral locations. The background color shows the topography as given in the ETOPO2 model (NOAA 2006). This and many of the subsequent figures have been made using the Generic Mapping Tools (Wessel & Smith 1995).

places, the Phuket province in Thailand (Titov et al. 2005). Had the earthquake slip propagated in the opposite direction along the Sumatra island, the tsunami height at Phuket would have been much smaller.

The occurrence of the 2004 Sumatra-Andaman earthquake challenged existing seismological techniques for monitoring and modeling seismic sources. An earthquake with a magnitude greater than 8.5 had not happened since the 1965 Rat Islands, Alaska, Mw 8.7 event (**https://earthquake.usgs.gov**), and initial estimates for the Sumatra-Andaman earthquake failed to capture its enormity. The magnitude estimate ranged between 6.2 and 9.0 within the first day, and a more realistic value of a magnitude above 9.0 was not obtained until many weeks later (Lay et al. 2005, Park et al. 2005). Detailed imaging of slip propagation during a given earthquake prior to the 2004 Sumatra-Andaman earthquake had been achieved only through finite-fault modeling, and the first set of finite-fault models showed the slip focused close to the epicenter, hence at Sumatra island, rather than extending nearly 1,200 km northward. These results led to confusion regarding the source and the magnitude of tsunami damage in Thailand, which should have been shielded by Sumatra. The inadequate estimates also caused the seismological community to aggressively improve existing approaches and design new methods that can reliably capture properties of great earthquakes. One of these techniques is back-projection analysis (Ishii et al. 2005).

The idea behind the back-projection method is simple (**Figure 2**). A conceptual analog is a snapshot of water ripples. A person can look at an image of circular water ripples in a pond and infer the location of the source of energy or where a pebble made contact with the water surface. In this case, the wavefront of the water ripple is visually collapsed to identify the point of contact. Similarly, the seismic wavefront observed by an array of seismometers can be collapsed or back-projected to find the source of energy. If multiple events occur simultaneously at different locations, they can be distinguished by examining how the different wavefronts arrive at the array (**Figure 2**).

The basic concept of time-reversing seismic data to determine the source of coherent waveforms has been used for decades in industry applications for imaging impedance contrasts in the

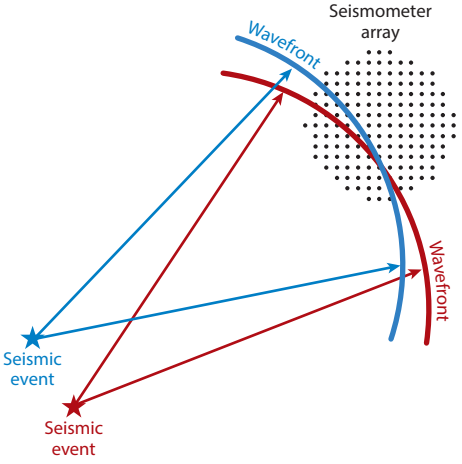

Figure 2

Conceptual idea behind the back-projection analysis. Wavefront (*red curve*) from a seismic event (*red star*) propagates through and is observed by an array of seismometers (*black circles*). The nonplanar nature of the wavefront allows it to be collapsed back to identify the source. If multiple events are occurring simultaneously (*red and blue stars*), they are distinguishable owing to the difference in how the wavefront is observed throughout the array.

subsurface (e.g., Claerbout 1976). Prior to back-projection, several studies applied this concept for locating earthquake sources using mostly local data sets. A common approach used recorded waveforms to numerically simulate time-reversed wavefields that, in theory, should collapse at the subsurface source location (e.g., McMechan et al. 1985, Rietbrock & Scherbaum 1994, Larmat et al. 2006). For high-frequency data, this approach is limited by inadequate knowledge of the small-scale velocity structure used for the wavefield simulations. Another common method called beamforming, which determines the slowness properties of planar wavefronts recorded at seismic arrays (e.g., Rost & Thomas 2002), has also been applied in several studies investigating the source of seismic waves and the structure of the earth (e.g., Spudich & Cranswick 1984, Earle & Shearer 1998, Kaneshima & Helffrich 1998, Hutko et al. 2006, Kito et al. 2008). Back-projection is similar to the beamforming approach, but it does not assume a planar wavefront. The plane wave assumption is used to determine a single back-azimuth direction (i.e., the direction toward the source) associated with the arriving packet of energy, but it often does not recover the distance information needed to identify the epicenter. The inclusion of wavefront curvature information in the back-projection analysis improves the ability to determine the source location, particularly when using large arrays (**Figure 3**).

Techniques that utilized array observations of curved wavefronts also existed prior to the 2004 Sumatra-Andaman earthquake, especially in the context of modeling events with seismometers located close to the source (e.g., Kao & Shan 2004). One aspect of the back-projection method that differs from these source modeling approaches is that the back-projection approach does not attempt to associate a particular waveform with a single source. Instead, a grid of potential source

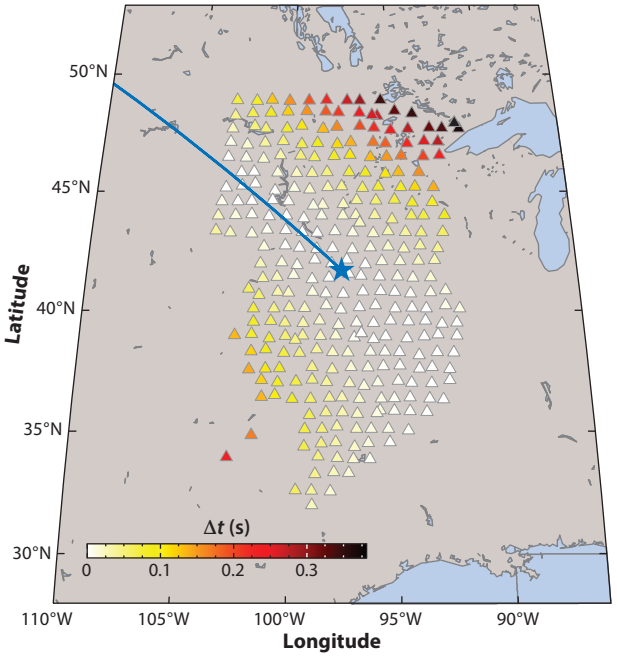

Figure 3

Difference between the travel times calculated for back-projection (*curved wavefront*) and the plane wave approximation for Transportable Array stations (*triangles*) with respect to the hypocenter of the earthquake on March 11, 2011, Tohoku-oki, Japan. The blue star is the center of the array, and the blue line is the back azimuth from the array to the hypocenter.

locations is set up in the region of interest, and the array data are systematically back-projected to each grid point (Ishii et al. 2005). This approach relies on constructive and destructive interference of the back-projected signal to establish the locations where the seismic energy originated. This strategy has two major advantages. First, it requires minimal a priori constraints for each analysis. Information such as fault geometry needed for finite-fault modeling is unnecessary. Second, it is simple. All that is required is the addition of data shifted to each grid point, and no matrix is inverted. This simplicity has probably contributed to the popularity of the method since its introduction. It also implies that the results are robust. Unlike finite-fault modeling results, the main features recovered through back-projection analysis are consistent between different research groups.

In addition to the independence from a priori constraints and simplicity, the back-projection method contains various features that are advantageous over other techniques. Because the collapsing of the wavefront is performed with travel times of a target seismic phase (e.g., the first-arriving P waves), there is an implicit slowness filter. This is particularly useful for large earthquakes for which additional unwanted seismic phases may arrive during the long source duration. For example, one of the reasons for the shortcomings of the initial finite-fault results for the 2004 Sumatra-Andaman earthquake comes from the arrival of PP waves. Because this earthquake took nearly 10 minutes to rupture from northwestern Sumatra to the Andaman islands, the surface-reflected PP waves arrived within the waveform of the direct P-wave train (Ni et al. 2005). To avoid contamination from the PP waves, initial finite-fault modeling efforts used data up to the expected arrival time of the PP waves, resulting in fault dimensions and an event magnitude that were underestimated. In contrast, the back-projection approach naturally removes other seismic phases such as PP from the P-wave analysis. The difference in slowness prevents PP waves from stacking coherently at the target source region using the P-wave slowness; in fact, they stack coherently almost midway between the source and the stations. The effects from unwanted phases can also be reduced if the frequency contents of the target and unwanted phases are different. For example, depth phases have slownesses similar to those of the direct P waves; however, because their paths sample near-surface structure with strong attenuation, they lose high-frequency energy compared with the direct P waves. Back-projection analysis can be applied to data filtered to any frequency range, which allows investigators to remove or suppress effects due to arrivals, such as the depth phases, even when they have similar slownesses.

The procedure of stacking seismograms at each grid point in the source region also implies that there is an azimuthal filter. Waves arriving from other azimuths, such as from earthquakes at other locations, are rejected through destructive interference. The use of a source grid also makes back-projection analysis suitable for the detection of multiple events. Unlike other approaches that determine the back-azimuth value, the blind stacking procedure unravels the waveforms and identifies simultaneously occurring earthquakes if there is enough resolution power in the data. Finally, the back-projection results can be, and have been, represented with attractive visual effects. The most successful of such effects is rupture propagation animations, which have been powerful communication and teaching tools.

One requirement of the back-projection analysis is the availability of an array of seismometers that allow data to interfere constructively and destructively through the stacking process. Deployment of both permanent and temporary dense networks of stations in recent years with open data access has aided in the development and advancement of back-projection analyses (**Figure 4**). High-quality data from these arrays are essential in obtaining detailed views of both giant and small earthquakes. As demonstrated below, the aperture and geometry of the arrays determine how well a given source can be resolved, and the denseness or spacing between seismic instruments controls the effectiveness of the stacking process. This manuscript provides an overview of the back-projection method with particular attention to the limits of the method.

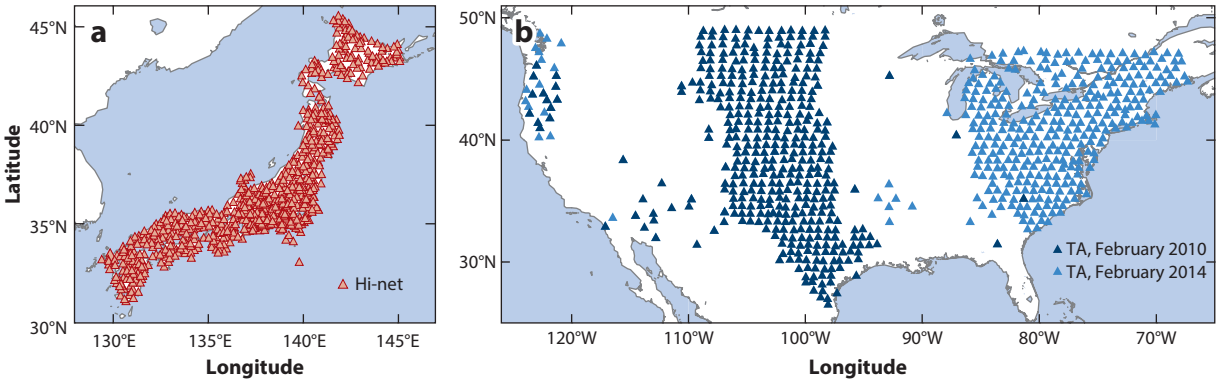

Figure 4

Examples of seismic arrays. (*a*) The High-Sensitivity Seismograph Network (Hi-net) of Japan (Okada et al. 2004, Obara et al. 2005). This network is a permanent network and consists of more than 750 seismic stations (*red diamonds*) distributed throughout the Japanese islands as of March 2015. The data are made freely available through the National Research Institute for Earth Science and Disaster Prevention. (*b*) The Transportable Array (TA) in the United States that consists of nearly 400 stations covering a narrow strip of longitude within the United States. The data are made freely available through the EarthScope USArray facility (operated by Incorporated Research Institutions for Seismology, supported by the National Science Foundation under Cooperative Agreement EAR-12,61681). This is a temporary array, and most of the stations are deployed for two years. The distribution of stations as of February 2010 (*dark blue triangles*) differs considerably from that of February 2014 (*light blue triangles*).

DESCRIPTION

In this section, we present an in-depth discussion of the back-projection method. This technique does have its own challenges, and some of these are described to clarify likely artifacts and possible future improvements. To illustrate successful implementations of the back-projection analysis, we provide some examples.

Method

For the back-projection method to successfully image earthquakes, the path effect, i.e., what happens to the seismic waves from the source to the seismic stations, must be known. This information can be obtained by sophisticated wavefield simulations, but these simulations are computationally expensive and detailed velocity models at relevant length scales are not always available. The problem is simplified by realizing that the first-order effect is the travel time, i.e., the time it takes for waves to propagate from one point to another, and that waveforms recorded at nearby stations are, in general, similar. On the basis of this recognition, back-projection analysis can be described by an equation of the form

$$s_j(t) = \sum_{i=1}^{N} w_{ij}(t)\, f_{ij}(t + \tau_{ij}), \qquad (1)$$

where $s_j(t)$ is a stacked time series dependent on time t associated with a source grid point j, summation is over N seismic stations, $w_{ij}(t)$ is a weighting function for station i and source point j, and f_{ij} is a function that describes the contribution of the ith measurement to the jth grid point. The time shift τ_{ij} gives the amount of time that is needed to send the information recorded at the ith station to the jth grid point. The name back-projection arises from this time reversal to the source region.

The simplest, and the original, approach to the propagation time τ_{ij} is to combine travel times calculated from a one-dimensional seismic model such as IASP91 (Kennett & Engdahl 1991) with empirical station-specific time corrections (Ishii et al. 2005). If we consider a seismogram recorded by the ith station, $u_i(t + \tau_{ij})$, within a network of N stations as the function $f_{ij}(t + \tau_{ij})$, the back-projected stack at the jth source grid point $s_j(t)$ is given by

$$s_j(t) = \sum_{i=1}^{N} w_{ij} u_i(t + \tau_{ij}), \tag{2}$$

where w_{ij} indicates weighting for each station i and grid point j, and τ_{ij} is the travel time between grid point j and station i. In this particular case, the weighted seismograms are linearly stacked to generate the stacked time series at various source points. Different forms of the function $f_{ij}(t + \tau_{ij})$ have been proposed and used. These include different stacking techniques (e.g., phase-weighted stacks; Schimmel & Paulssen 1997), measures of coherency between recorded signals (e.g., Ishii 2011), and correlation between theoretical Green's functions and recorded signals (e.g., Yagi et al. 2012). These functions are designed to enhance certain features of interest. For example, the linear stacking approach is useful when one is interested in the relative seismic energy radiation as a function of time and space. On the other hand, this approach can be dominated by the largest signal and is not suitable for detecting smaller events occurring at similar times and locations (**Figure 5**). To identify events, a more appropriate function is one that measures similarities of waveforms (e.g., coherency).

One vital component of the back-projection approach is the time shift τ_{ij} that time-reverses the functions to the source locations. In principle, this measurement can be calculated using a

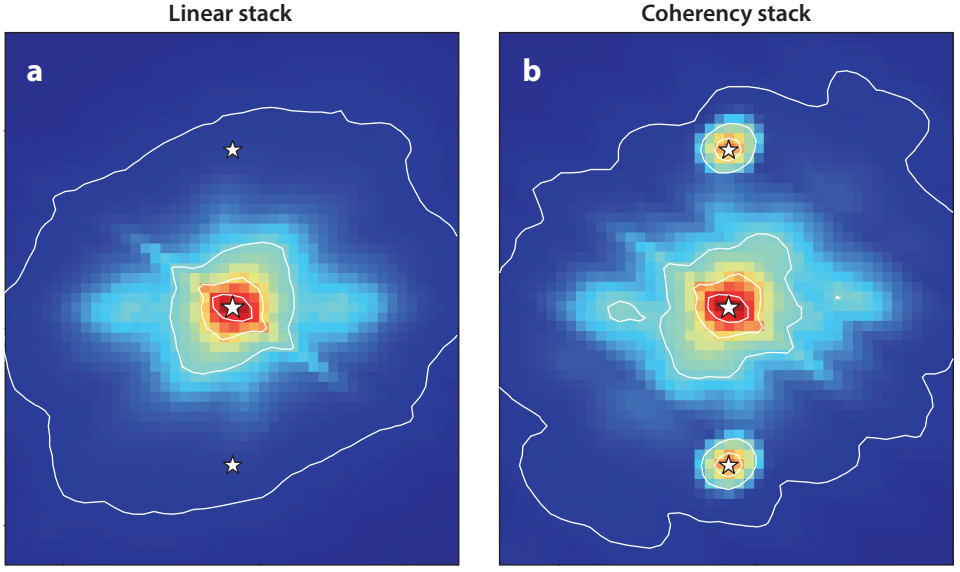

Figure 5

Comparison of linear and coherency stack back-projection results. Synthetic data are generated from three point sources occurring 10 s apart (the north/south sources occurring 10 s after the central source) with different amplitudes (north/south sources have 10% of the amplitude of the central source). (*a*) Result from linear stacking with three stars showing the input point source locations. The background color shows the stacked amplitude, with warm colors showing high amplitude. (*b*) Same as in panel *a* except that coherency is used as the function that is being stacked.

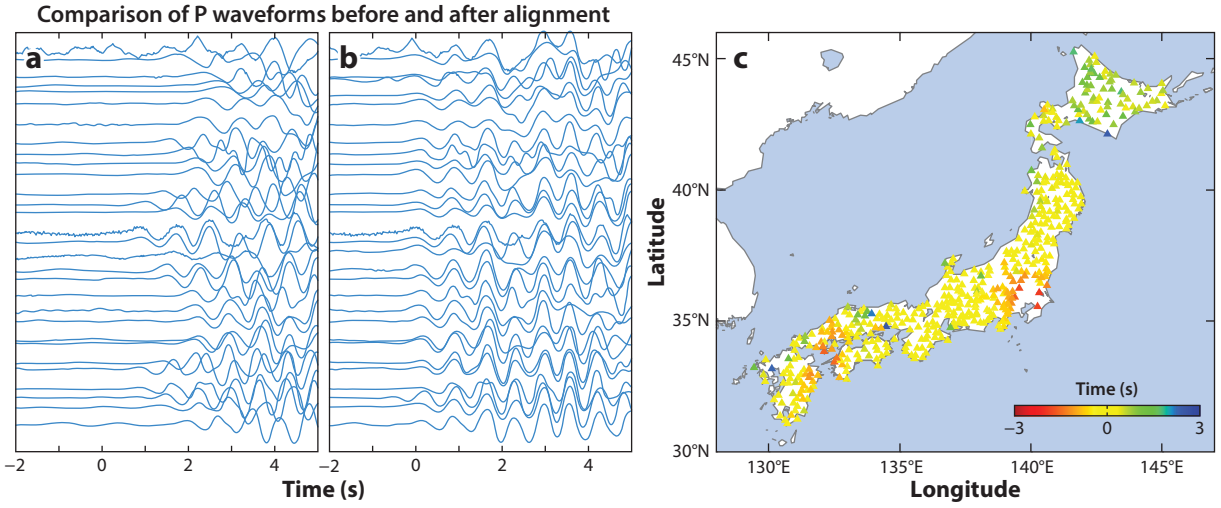

Figure 6

Empirical time corrections. (*a*) Seismograms of a subset of stations from the High-Sensitivity Seismograph Network (Hi-net) of Japan showing the P-wave arrival from the 2004 Sumatra-Andaman earthquake. Note that time is with respect to the predicted P-wave arrival time using a one-dimensional Earth model, IASP91 (Kennett & Engdahl 1991). (*b*) Same as in panel *a* after cross correlation has been performed to align the seismograms. (*c*) Distribution of empirical time corrections at Hi-net stations (*colored triangles*). The colors indicate the time correction in seconds.

three-dimensional model of the Earth's interior and a method for determining travel times of a given seismic phase through such a model (e.g., wavefield simulation or ray tracing). However, back-projection analysis is often performed using relatively high-frequency data for which the three-dimensional model is often not adequate. The time corrections are, therefore, usually separated into two parts, theoretical and empirical, as described in the previous paragraph. The first contribution determines the propagation time between source grid point and station on the basis of a given model such as a one-dimensional Earth model. The second correction aims to account for insufficiency in the theoretical prediction using empirical observations. In the above example, τ_{ij} consists of the travel time between grid point j and station i based on a one-dimensional model (i.e., dependent only on distance) $\Delta\tau_{ij}$ and an empirical correction for the source-station path $\delta\tau_{ij}$ such that $\tau_{ij} = \Delta\tau_{ij} + \delta\tau_{ij}$. If the empirical correction is obtained by cross correlation of waveforms recorded throughout the array, small station spacing and similar ray paths (i.e., an array size that preserves waveform similarity) are desirable (**Figure 6**). The empirical time correction, even though it is much smaller than the theoretical component, is crucial for obtaining a high-quality image at the source. If the empirical corrections are inaccurate, the back-projected stacks can produce blurred images or erroneous sources.

Ideally, the time shift τ_{ij} is available for every path between source grid j and station i. If the values are computed purely theoretically, this ideal scenario is easily achieved. However, when the time shift is separated into theoretical and empirical components, it is practically impossible for investigators to determine empirical time corrections between every grid point and station path because doing so requires having a seismic event at every grid point. One could attempt to achieve spatial coverage by combining empirical corrections obtained by analyzing seismograms from other earthquakes in the source region (Ishii et al. 2007). This introduces bias into the problem because time shifts obtained empirically are not necessarily consistent from event to event. One approach that is often embraced is to use a single reference event to determine the empirical

component of the time correction. Another approach to the problem is to make slowness corrections at each station that can complement empirical travel time corrections (Meng et al. 2016).

When an empirical approach is used to obtain the time correction, certain information becomes lost. For example, cross correlation of waveforms provides time shifts required to align the seismograms, but this is with respect to a reference trace. The timing is, therefore, relative to this reference trace. To understand the loss of absolute time information, consider adding a constant to the time shift values obtained through cross correlation. The seismogram waveforms are still aligned with one another, but the time is different. Hence, time information in back-projection results is usually given with respect to some reference time. Another effect of the empirical time correction is its association in space. Perturbations in wave arrival times come from the complex structure within which the wave travels, but they also contain uncertainties in the hypocentral location and time. These two contributions are difficult to separate, leading to a loss of absolute location information. The empirical time corrections are often obtained using the initial few seconds of the first-arriving P waveforms, and hence the aligned seismograms are associated with the hypocentral location. Changes in source locations observed through the back-projection analysis are, therefore, with respect to this reference location.

The final ingredient of the back-projection analysis is the weighting scheme $w_{ij}(t)$, which can take various forms. The main purpose of this weighting is to control the contribution of each function to the final stack. For example, when summing the seismograms, it may be desirable to normalize each seismogram such that no single trace dominates the stack. An appropriately designed weighting scheme can also reduce bias in the back-projected result. For example, a point source is not perfectly recovered as a point source, and the shape of the smeared image (resolution kernel) depends on the geometry of the array used in the analysis (**Figure 7**). This array-shape resolution can be suppressed by applying a spatially dependent weighting scheme that tapers down from the center of the array to its edges as to mimic a circular array. A time-dependent weighting

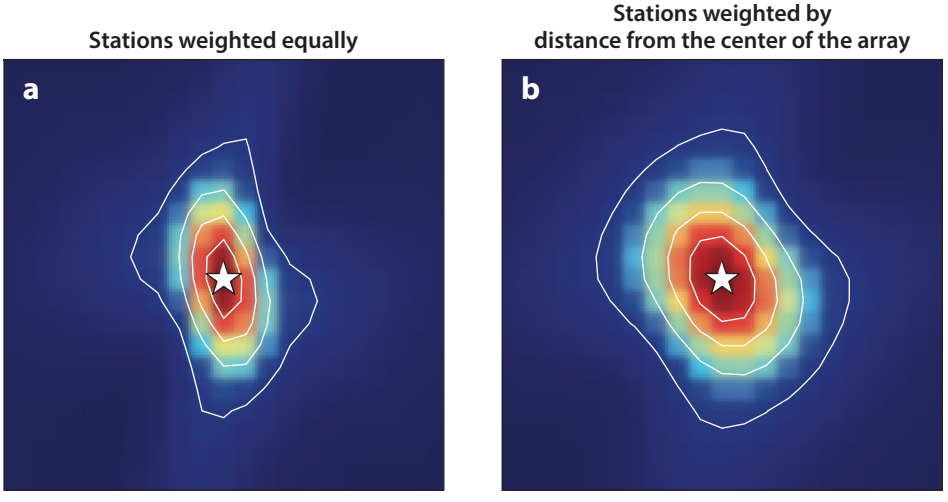

Figure 7

Effect of spatial weighting demonstrated through the use of synthetic data generated using a point source (*white star*). The background color shows back-projected amplitudes, with warmer colors indicating higher values. (*a*) Back-projected image obtained using the Hi-net array geometry with stations weighted equally. (*b*) Same as in panel *a* except a filter that mimics a circular array geometry is applied, i.e., each station is weighted differently on the basis of their distance from the center of the array. The resolution becomes more symmetrical.

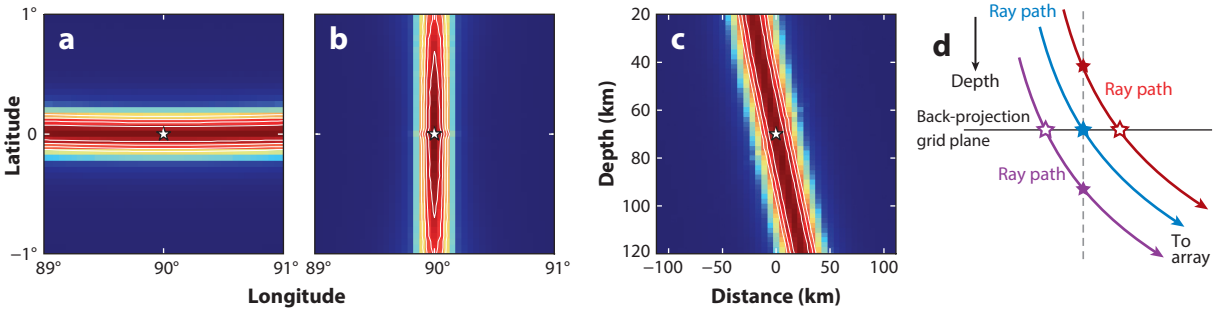

Figure 8

Effects of imperfect data coverage. Synthetic seismograms are generated using an input source (*white star*) for a set of 300 stations located north of the source. Warmer colors indicate higher recovered amplitude. (*a*) Back-projection result using synthetic data from a hypothetical array at a constant azimuth but covering 30° in distance between 40° and 70° with respect to the input source location. The plot shows an area that is 2° longitude by 2° latitude. (*b*) Same as in panel *a* except that the stations are positioned at a constant distance but have an azimuthal range of 30° between −15° and 15°. (*c*) Same as in panel *b* except that the stacks are visualized as a depth cross section along the direction toward the array. (*d*) A diagram showing the bias in location of events (*solid red and purple stars*) when the source grid defining the horizontal plane (*blue line*) based on a reference event (*blue star*) is used. Due to smearing along the ray path as shown in panel *c*, the events are mislocated in space and time (*open red and purple stars*).

scheme can also be used to emphasize features within each time window of interest (e.g., Kiser et al. 2011, Meng et al. 2011, Yao et al. 2012).

Artifacts and resolution. Because the data coverage is never perfect, the back-projection analysis always introduces uncertainties in space and time (e.g., Ishii et al. 2007, Kiser & Ishii 2012a), and back-projecting a set of synthetic data generated from a point source will fail to recover the point source. Instead, the location and timing of the smeared back-projected result depend on the size and geometry of the array used in the analysis (**Figure 8**). This array response can be understood as arising from two limitations. If the array has good distance coverage with limited azimuthal coverage, the distance to the source location is well-constrained. However, the azimuth of the source with respect to the array is poorly determined, resulting in a back-projected image that has large uncertainty in the source location in the direction perpendicular to the ray path toward the array (**Figure 8*a***). Similarly, if the azimuth is well-covered by the array but the distance is not, the resulting resolution constrains the azimuth of the source well but poorly constrains its distance (**Figure 8*b***). The level of spatial smearing also depends on the type of seismic phase used in the analysis. If a phase has nearly constant slowness with distance (e.g., inner-core reflected P waves, PKiKP), the wavefront is nearly planar, resulting in a point source that becomes linearly blurred.

The spatial smearing observed in these examples is from imperfect constructive and destructive interference due to limited azimuth and/or distance coverage. Away from the point source location and time, the back-projected quantity (e.g., normalized traces) misaligns and interferes destructively, and the constructive interference degrades gradually along the ray away from the hypocenter. In a map view, the slow degradation of constructive interference appears as energy moving toward the array, and in the depth direction, the smearing follows the ray path and speed of the seismic phase used in the analysis (**Figure 8*c***). For example, if the first-arriving P waves are used in the analysis, the back-projected energy tends to move toward the array along the P-wave ray path at P-wave speed. This artifact appears as a supershear rupture at the source, and such observations should be interpreted with utmost caution. The smearing along the ray path also implies that when teleseismic observations are used in the analysis, depth resolution will be

poor, owing to the steep takeoff angle of waves. For this reason, the depth dimension is often ignored and rupture propagation on a horizontal plane is considered (e.g., Ishii et al. 2005). This projection onto a horizontal plane introduces bias in event location and timing (**Figure 8*d***). If an event occurs at the same depth as that of the source grid, then the location and timing of the event should match those recovered from the back-projection analysis. However, if an event occurs at the same epicentral location but at a shallower depth, then the back-projected energy will place it at a location that is offset toward the array at a time that is later than the actual hypocentral time. If an event occurs at a deeper depth, then the location is biased away from the array with earlier timing. These relationships are reversed when using seismic phases that propagate upward from the source (e.g., pP).

The spreading of a point source imposes a spatial threshold above which rupture propagation of an earthquake can be imaged. If the rupture is confined within the point-spread function, rupture propagation cannot be observed. For example, using the Hi-net array in Japan (**Figure 4**) for the Sumatran subduction zone and simple linear stacking of seismograms, rupture propagation can be resolved for earthquakes with magnitudes greater than 7.7. To determine detailed earthquake processes, a small point-spread function is therefore desirable. Aside from setting up a larger array with better azimuth and distance coverage (which may be difficult to achieve), there are multiple approaches with which the resolution can be improved. One could attempt to remove the array response from the back-projected stacks, but this step requires assumptions to calculate array responses (Lay et al. 2009). Furthermore, this procedure can lead to unstable results because the array response can be thought of as the null space of the inverse problem. Alternatively, noting that the artifacts have features that depend on the azimuth of the array, back-projected images can be sharpened using multiple arrays (**Figure 9**). If arrays that are located at considerably different azimuths with respect to the source region can be found, then the point-spread functions (array response or resolution kernel) from the arrays are consistently high at the true source location. All other high-amplitude features of the array responses do not have consistent locations and timings, thus improving the resolution of the combined result. This array combination approach should be performed with care. For example, to recover reliable spatiotemporal information, the data from a given array should be back-projected to the source region before being combined with stacks from different arrays. Because the time information is relative and each array may be referenced to different times, the stacks should be compared at the spatial reference point (e.g., hypocenter) and aligned before being combined (Kiser & Ishii 2012a).

One source of concern, when combining different arrays, is the effect of directivity. For very large earthquakes or for dense arrays located close to the source region, the distortion in the recorded waveforms due to rupture propagation varies depending on the station location with respect to the propagation direction. To account for this effect, the waveforms can be stretched or shrunk before analysis. However, this step requires an a priori knowledge of rupture propagation direction as well as assumptions about the complexity of the rupture. This approach is not desirable for back-projection analysis because the a priori conditions or assumptions, if they are incorrect, will map into results. Furthermore, if an array is large enough to provide reasonable resolution near the source (i.e., if the resolution kernel or array response dimensions are much smaller than the length dimension of the earthquake rupture), the back-projection analysis can identify the rupture location and timing, even when the rupture propagates in multiple directions (**Figure 10**). Application of a stretching function to observed waveforms is, therefore, unwarranted and will lead to artifacts. By comparison, directivity does affect the relative amplitude of the seismograms used in back-projection analysis. If the array is positioned in the direction of rupture propagation, the amplitude is overestimated and vice versa. This effect must be considered when interpreting relative amplitude results from back-projection analysis.

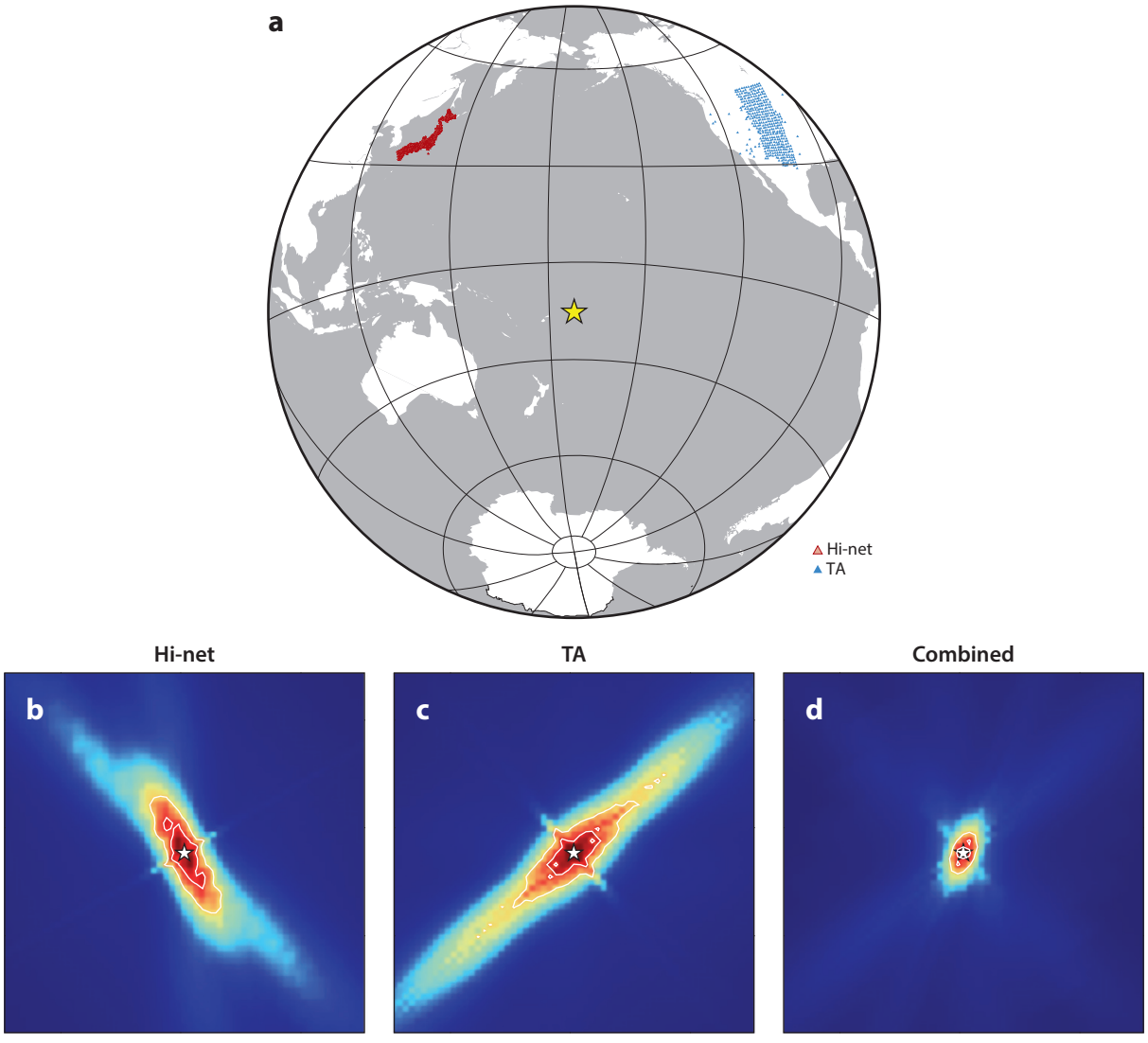

Figure 9

Approaches to improve back-projection resolution using multiple arrays. The synthetic data are generated for the High-Sensitivity Seismograph Network (Hi-net) of Japan and the Transportable Array (TA) in the United States (geometry as of September 2009) using a point source at an epicentral location shown by the star in the Samoa region in the southern Pacific. (*a*) Locations of the point source (*yellow star*), TA (*blue triangles*), and Hi-net (*red triangles*). (*b*) Back-projection result using synthetic Hi-net data in an area around the epicenter that is 3° by 3°. Warmer colors show higher amplitudes. (*c*) The same as panel *b* with TA data. (*d*) Combined result when stacks from panel *b* and panel *c* are added.

Similar to combining two azimuthally distinct arrays to improve azimuthal resolution, resolution in the depth direction can be improved by combining arrays at different distances. An array at a large distance observes rays that take off downward, whereas data recorded by a nearby array consists of rays traveling upward (**Figure 11**). Because the smearing in the point-spread function is along the ray path, the small region within the smeared images that consistently shows large

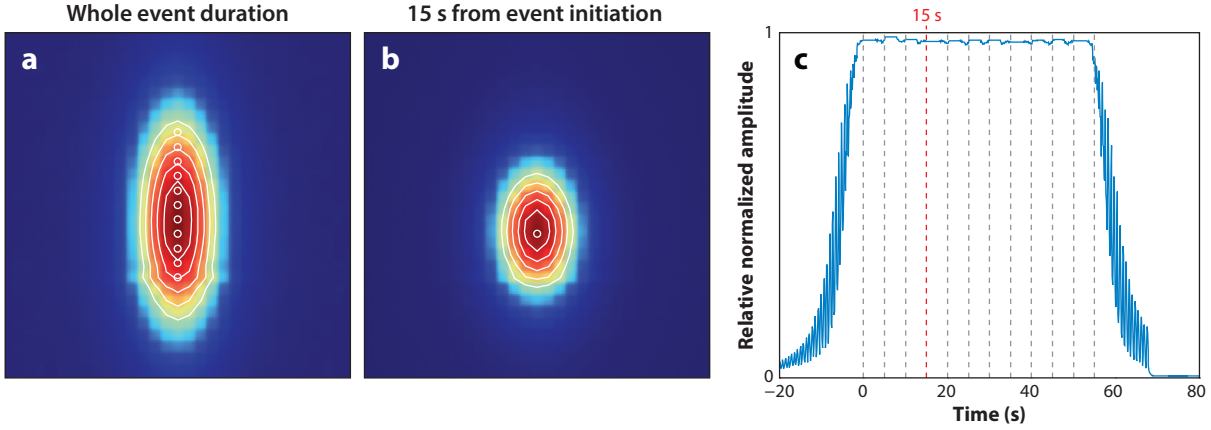

Figure 10

Demonstration of the directivity effect. Synthetic data are generated from 11 sources at a 5-s interval, imitating unilateral rupture propagation from south to north with a rupture speed of 2.8 km/s. (*a*) Map view comparison of input locations (*white circles*) and recovered image (*background color*; *warmer colors correspond to a higher coherency value*). The area depicted in this plot is 3° by 3°. Time integration is performed over the whole duration of the event and captures the area that ruptured. (*b*) Same as in panel *a* except that it is a time snapshot at 15 s from event initiation rather than for the entire event. The input corresponding to this time (*white circle*) is consistent with the peak of the background color. (*c*) The coherency value as a function of time with respect to the first input source timing (*blue curve*). The dashed vertical bars show the timing of the input sources; the red line corresponds to the time shown in panel *b*.

amplitude, regardless of the array used, should be the true source. For most earthquakes around the world, however, it is fortuitous to have a local array positioned within a very small distance range. Alternatively, depth resolution can be improved with data from a single array using seismic phases with different takeoff angles. For example, the direct P and depth phases (e.g., pP and sP) leave the source region downward and upward, respectively, providing coverage in the takeoff angles needed for good depth resolution (**Figure 11**). Similar to multiple-array stacking, different phases of interest should be back-projected to the source grids individually before being combined. The requirement for this procedure to work is either that the phases are well separated from one another in time or that their slownesses are distinct enough to avoid coherent stacking in the source region. If the direct P phase is combined with one or two of the depth phases, then the slownesses are similar to one another; hence the phase-combination technique improves the depth resolution of only deep earthquakes (e.g., depths below 100 km) for which the phases are clearly separated in time. Finally, depth resolution can also be refined by defining the function $f_{ij}(t)$ in Equation 1 to be something that incorporates effects due to depth such as comparisons with Green's functions that include direct and depth phases (e.g., Yagi et al. 2012).

Utilization. The back-projection analysis of array data is robust in that it requires a limited number of assumptions and involves no inversion. It is also flexible in the types of data that can be used in the analysis. Different body waves such as P waves and S waves or surface waves can be utilized, depending on the type of constraints desired or data available. The data can also be filtered to different frequency bands to investigate the frequency dependence of the earthquake rupture process. For example, the first-arriving P waves can be filtered to different frequency ranges and back-projected to the source. High-frequency waves provide better temporal and spatial resolution than lower-frequency waves. Therefore, analysis using high-frequency arrivals is desirable, and the high-frequency limit for back-projection analysis is dictated by the level of

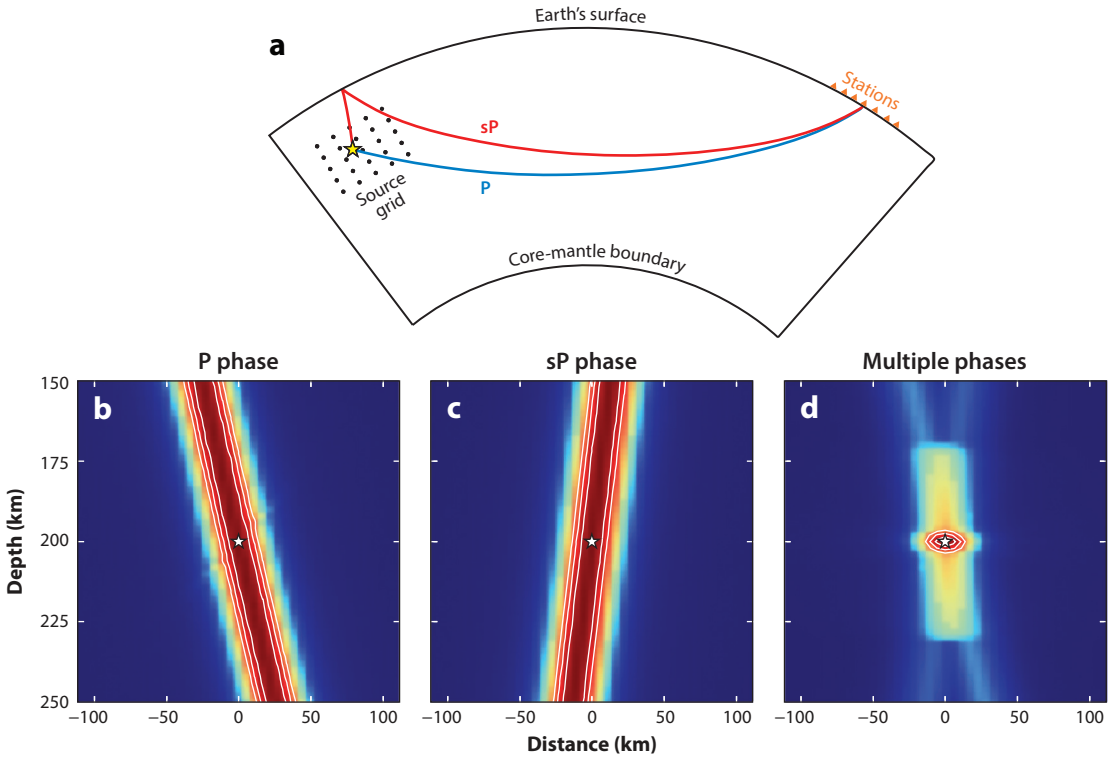

Figure 11

Improvements in depth resolution using multiple phases. Synthetic data generated from a point source at a depth of 200 km is used to demonstrate the smearing effects. The synthetic seismic array is the same as **Figure 8*c***. (*a*) Comparison of ray paths between direct P (*blue curve*) and a depth phase, sP (*red curve*), through the Earth in a cross-sectional view. The source grid is set up in three dimensions (*black dots*) around the hypocenter (*yellow star*). The phases are recorded by an array of stations (*orange triangles*). (*b*) Resolution as a function of depth and distance toward the array obtained by back-projecting the P waveforms to the source region. The white star is the input source location. Smearing occurs along the ray path. (*c*) Same as in panel *b* except using the sP phase instead of P. (*d*) Improved resolution with the combination of the P and sP phases.

attenuation the data experience and the level of scattering that degrades the waveform similarity. Depending on the array distance and structure along the ray paths, the data above some frequency simply contain noise. In contrast, low-frequency signals are typically less affected by attenuation and scattering structure and can be observed when high-frequency contents have decayed away. However, lowering the frequency content of a given seismic wave leads to an increase in the wavelength, resulting in a point-spread function that is much broader than if the same data are filtered to a higher frequency (**Figure 12**).

The back-projection analysis is particularly suitable for obtaining relative information such as relative location and timing. If a certain form of $f_{ij}(t)$ is used, a rough measure of relative radiated energy can also be estimated. However, the results cannot be related directly to absolute measures such as the amount of slip at a given location or overall magnitude of the event. To convert back-projection results into these parameters, one could make assumptions and invoke empirical relationships. For example, in the study of the 2004 Sumatra-Andaman earthquake, the authors used the area of the rupture obtained from back-projection analysis and combined it with an empirical relationship between slip area and magnitude to estimate the event magnitude to be

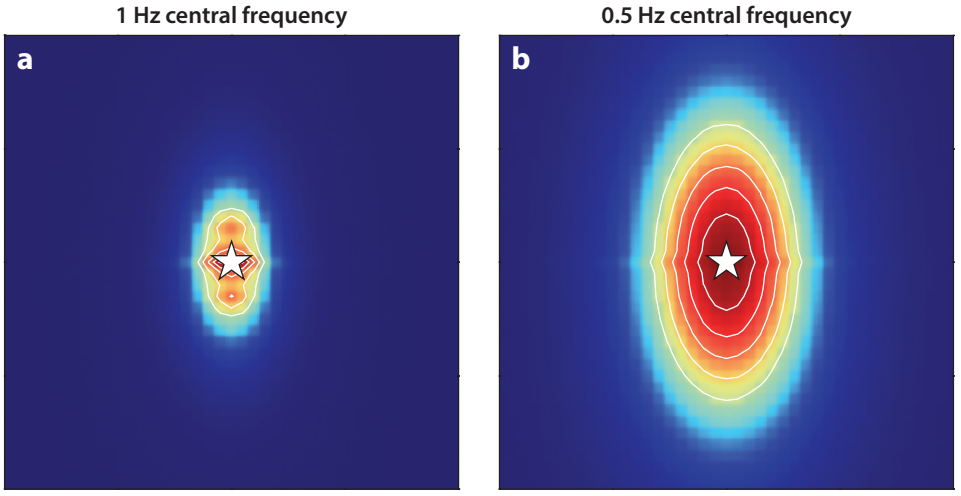

Figure 12

Frequency dependence of resolution. Synthetic data are generated using a point source for 345 stations that make up a nearly circular array; its center is located 60° due north. The area shown is a 4° by 4° space around the epicenter of the input source. (*a*) Resolution at the source from a point source (*white star*) that has a source-time function of a Ricker wavelet with a central frequency of 1 Hz. (*b*) Same as in panel *a* except a central frequency of 0.5 Hz is used.

approximately 9.3 (Ishii et al. 2005). Such conversions introduce additional uncertainties and are often not undertaken. Back-projection results are typically presented as relative information.

Applications

The back-projection method was initially developed to image detailed rupture propagation of giant earthquakes, but its flexibility has allowed its use for smaller earthquakes and event detection. In the following subsections, we describe some examples of the use of the technique mainly from our work. We focus on the results obtained from the back-projection analysis and, in many cases, omit or only briefly discuss interpretation of the results.

The use of back-projection for source analysis is becoming popular, and various research groups have employed different flavors of the approach with interesting results. A few events that have garnered significant attention from the back-projection community include the 2004 Mw 9.3 (Ishii et al. 2005, 2007; Lay et al. 2012), 2005 Mw 8.6 (Ishii et al. 2007, Lay et al. 2012), 2007 Mw 8.5 (Kiser & Ishii 2012a, Lay et al. 2012), and 2012 Mw 8.6 Sumatra earthquakes (Meng et al. 2012, Wang et al. 2012, Yue et al. 2012, Ishii et al. 2013); the 2010 Mw 8.8 Maule, Chile, earthquake (Lay et al. 2010b; Kiser & Ishii 2011, 2012a; Wang & Mori 2011, Koper et al. 2012); the 2011 Mw 9.0 Tohoku-oki earthquake (Ishii 2011, Koper et al. 2011, Meng et al. 2011, Yao et al. 2011, Kiser & Ishii 2012b, Roten et al. 2012, Yagi et al. 2012, Yao et al. 2012); the 2013 Mw 8.3 Sea of Okhotsk deep-focus earthquake (Ye et al. 2013, Meng et al. 2014); and the 2015 Mw 7.8 Nepal earthquake (Avouac et al. 2015, Fan & Shearer 2015, Grandin et al. 2015, Yagi & Okuwaki 2015, Meng et al. 2016). Many of the advances made to the back-projection method were developed to better understand the rupture properties of these earthquakes, and interested readers should reference these studies for the descriptions and motivations behind modifications to the original back-projection method.

Rupture properties of earthquakes. A magnitude 8.8 subduction-zone earthquake occurred near Concepcíon, Chile, south of Santiago on February 27, 2010. This segment between the northern end of the 1960 Mw 9.5 earthquake and the southern end of the 1985 Mw 8.0 Valparaiso event has been known as a seismic gap where a large thrust earthquake had not occurred since the 1835 earthquake documented by Charles Darwin aboard HMS Beagle (Darwin 1845). The earthquake of 2010 was well recorded by the Transportable Array in the United States, consisting of 390 stations (**Figure 4**). This temporary array covered a strip in the middle of the United States that extended from the northern border with Canada to the southern border with Mexico. The distances between the 2010 Chile event and the stations of the Transportable Array were well within the P-wave arrival window.

When the P waves are filtered to a relatively high-frequency range between 0.8 and 2.0 Hz, the back-projected images clearly show the propagation of rupture associated with this event (e.g., Lay et al. 2010b, Kiser & Ishii 2011, Wang & Mori 2011, Koper et al. 2012). The rupture initiates at the epicenter and propagates both north and south (i.e., bilateral rupture) for about 150 s (**Figure 13**). The back-projected locations of energy release are mostly downdip of the epicenter, suggesting that the rupture propagates deeper on the plate interface. The northern component of the rupture is divided into two parts, starting with a subevent close to the epicenter. When rupture from the epicenter reaches a latitude of about 35°S at about 45 s from the start of the earthquake, it appears to terminate and jumps updip before continuing on the second part of the northern rupture (**Figure 14**). In contrast, the southern component of rupture shows only weak energy release, peaking at about 80 s from event initiation. This difference in amplitude is likely to be associated with

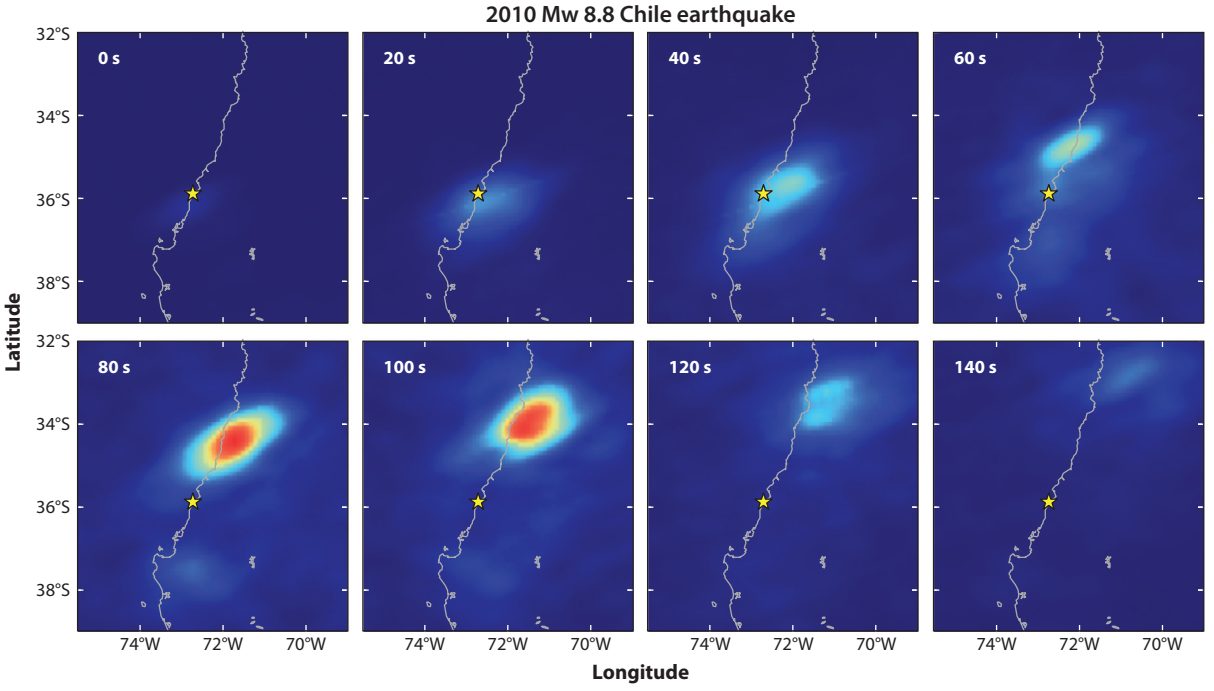

Figure 13

Back-projected images of the 2010 Mw 8.8 Chile earthquake at different times shown in the top left corner of each panel (seconds with respect to the hypocentral time). The yellow stars show the epicentral location, and the gray curves show the coastline.

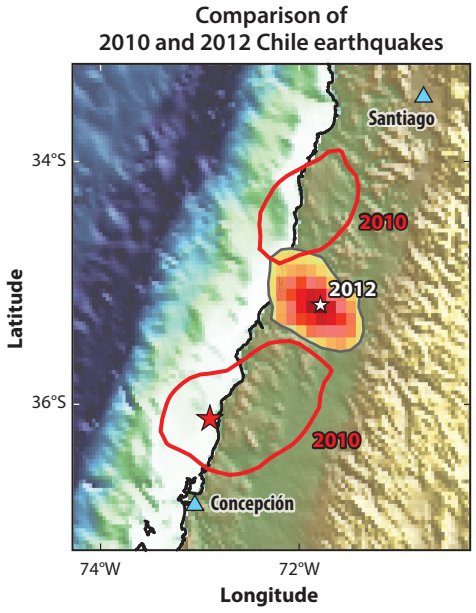

Figure 14

Red contours show the two northern portions of the rupture propagation for the 2010 Mw 8.8 earthquake from back-projection analysis; the red star shows the epicenter. There is a gap around 35.5°S, which is filled by the Mw 7.1 earthquake on March 25, 2012 (*colored area with gray outline*). The white star shows the epicenter of the 2012 earthquake. Two cities, Santiago and Concepción, are shown by blue triangles. The background colors show topography of the region using ETOPO2.

the directivity effect because the azimuth toward the Transportable Array is north (**Figure 10**). The northern rupture is moving toward the array, hence the amplitudes can be overestimated, while the southern rupture is moving away from the array, leading to underestimated amplitudes.

Closer inspection of stacked amplitudes indicates that there is a peak in energy release as the rupture reaches the end of both the first and second northern subevents. These bursts can be related to rapid deceleration of slip as it terminates at the end of a fault segment. These theoretically proposed "stopping phases" (Spudich & Frazer 1984) are also consistent with the subsequent gap in rupture between the northern subevents (**Figure 14**). This gap in high-frequency energy radiation also corresponds to an area of reduced aftershock occurrences compared with the rest of the source area. Subsequently, the largest thrust aftershock of the 2010 Mw 8.8 earthquake occurred in this region on March 25, 2012, about two years following the mainshock. The magnitude of this event was 7.1, and back-projection analysis shows that it ruptured an area that covers the gap observed during the 2010 mainshock (**Figure 14**). All these observations agree with the notion that the plate interface is segmented and that ruptures can jump over a segment to trigger a slip on another segment. They also support the idea that earthquakes may grow to their large sizes because cascading can trigger multiple fault segments.

The direct P waves observed at the Transportable Array stations contain energy at frequencies lower than the 0.8 to 2.0 Hz used in the above analysis; likewise, if they are filtered to a range between 0.05 and 0.1 Hz, the back-projected images show considerable changes. Spatial resolution is poorer due to longer wavelengths at lower frequencies; however, contrary to the high-frequency results, overall energy release is larger to the south of the epicenter (**Figure 15*a***). This difference

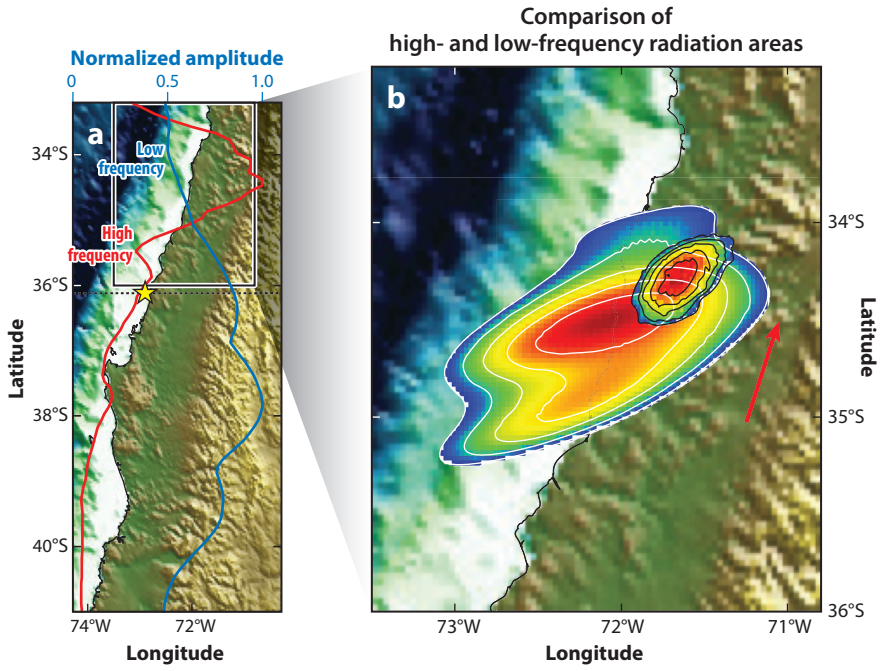

Figure 15

Frequency dependence of back-projected images from the 2010 Mw 8.8 Maule, Chile earthquake. (*a*) Comparison of peak normalized amplitude (*upper scale in blue text*) as a function of latitude from back-projection results using data filtered to high-frequency (*red curve*) and low-frequency (*blue curve*) ranges. Topography (ETOPO2) is shown in the background with the epicenter (*yellow star*) and its latitude (*dashed black line*), along with a region bound by a box corresponding to the area shown in panel *b*. (*b*) Comparison of the locations of back-projected high-frequency (*small colored area with black contours*) and mid-frequency (*large colored area with white contours*) stacks between 70 and 100 s since event initiation. The red arrow indicates rupture propagation direction (offset in longitude for clarity).

in the peak amplitude location suggests that the southern segment is dominated by slower slip compared with the northern segment. Furthermore, in the northern rupture where both high- (1 to 5 Hz) and mid-frequency (0.5 to 1 Hz) signals are cleanly visible, the location and timing of the two signals have interesting properties. Even though the lower-frequency results suffer from poorer spatial resolution, the stacks show rupture occurring updip and behind high-frequency energy locations (**Figure 15*b***). These observations are consistent with the hypothesis that high-frequency energy is dominantly released as the fault breaks at the leading edge of the rupture followed by a more gradual slip on the fault plane.

Comparison of the back-projected results with those from finite-fault modeling shows similarities and differences (e.g., Koper et al. 2011). The basic features of the event, e.g., bilateral rupture propagation, duration, and a gap at around 35°S, are observed from both modeling approaches. However, most slip obtained in finite-fault modeling occurs updip, sometimes extending to the trench, farther offshore than where the high-frequency back-projection analysis shows sources of energy. The spatial offset can be partly attributable to the uncertainty in the reference location (the hypocentral location) used in the back-projection analysis, but this effect is not large enough to explain the difference. The back-projection analysis, even by itself, showed changes in the results using different frequency contents; lower-frequency signals placed sources updip of

high-frequency results. Finite-fault models are typically based on even lower frequency data such as S waves and surface waves, suggesting that the observed disagreement between back-projection and finite-fault results is due to frequency dependence. This frequency dependence is observed for other great earthquakes (e.g., 2011 Tohoku-oki, Japan, earthquake; Koper et al. 2011, Wang & Mori 2011, Yao et al. 2011, Kiser and Ishii 2012b), and Lay et al. (2012) have proposed a model of plate interface properties and typical slip behavior at subduction zones.

For earthquakes such as the 2010 Chile and 2004 Sumatra-Andaman events, which are thought to have had a relatively simple rupture on a plane, finite-fault modeling provides valuable insight into slip behavior. However, if an earthquake occurs with complex rupture behavior, then finite-fault modeling may not be the best approach due to its dependence on a priori constraints, especially the geometry of the fault plane. The back-projection analysis, in contrast, requires little a priori information, where the geometry or location of the fault plane is not needed. It is, therefore, a suitable method for investigating earthquakes with any level of rupture complexity.

A magnitude 8.6 earthquake that occurred off Sumatra island in 2012 is an example of an elaborate rupture pattern that challenged finite-fault modeling. The epicenter was located well within the Indo–Australian plate, about 200 km from the closest plate boundary (Sumatra trench). It was also a strike-slip event, and the unusually large magnitude makes it the largest strike-slip earthquake ever recorded (e.g., McGuire & Beroza 2012). The earthquake started out as a bilateral event on a fault that is oriented southeast to northwest, switched to a rupture propagating toward the Sumatra trench on a fault almost perpendicular to the initial orientation, jumped over to a segment that is farther away from the trench than any previous rupture, propagated unilaterally in the northwest direction, made another jump at the Ninety-East Ridge, and had a final subevent on this ridge that appears to have had a northern rupture propagation (**Figure 16**). This event is a clear case of a giant earthquake that involved breakage of multiple faults. At least four fault segments, some perpendicular to one another, were involved (e.g., Meng et al. 2012, Wang et al. 2012, Yue et al. 2012, Ishii et al. 2013). This type of complex behavior is extremely difficult to capture using the conventional finite-fault modeling methods alone.

Because the back-projection analysis is relatively simple and provides information that is complementary to constraints from finite-fault modeling, it is becoming a standard tool with which to investigate earthquake ruptures, especially of giant events. For example, automatic P-wave back-projection results of large earthquakes using arrays around the world are one of the products at the Data Services of the Incorporated Research Institutions for Seismology and are readily accessible via Internet query (Trabant et al. 2012). Because earthquakes can occur at any time, high-quality permanent arrays such as the Hi-net array in Japan are most desirable. Temporary arrays such as the Transportable Array in the United States have been contributing significantly to the analysis of recent great earthquakes, but they will not be available for future events. One could group a collection of independent seismic stations within a given region to make an array. Stations in Europe are often grouped together in this manner to form an array for back-projection, and the automatic solutions provided by the Incorporated Research Institutions for Seismology often use this pseudoarray. One potential issue is that these aggregate arrays typically consist of different instruments and may require additional data-processing techniques.

Intermediate-depth earthquakes. In a second set of examples, we now describe results from a study based on an approach to improve depth resolution using a combination of direct and depth phases (e.g., Kiser et al. 2011). For earthquakes discussed in the previous section, the resolution in the depth dimension is so poor that it has been ignored and the results are those of a projection onto the hypocentral depth plane. For these shallow earthquakes, depth phases, which have slownesses similar to that of the direct P waves, cannot be reasonably separated from the direct phase;

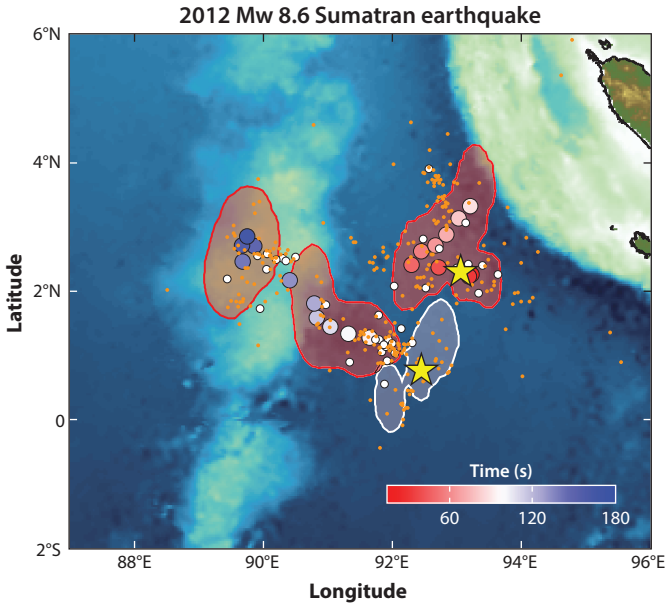

Figure 16

Summary of the back-projection result for the 2012 Mw 8.6 Sumatran earthquake showing the complex rupture pattern. The regions colored and outlined by red show different parts of the rupture. The colored circles within these regions are the rupture locations as a function of time as shown by the color bar. The white area indicates the rupture area that was inferred from a back-projection analysis of the Mw 8.2 earthquake that followed the Mw 8.6 event by 2 h. Yellow stars show the epicentral locations of the two earthquakes. Orange dots and white circles show aftershock locations that occurred in the first 7 days and between the two mainshocks, respectively.

hence the phase-combination approach does not work well. However, if earthquakes occurring at considerable depths are investigated, the time separation of the phase arrivals becomes large enough to treat them independently. In this section, we focus on intermediate-depth earthquakes, events occurring at depths between 100 km and 400 km, that are recorded by a dense, high-quality array (i.e., the Hi-net array in Japan) at teleseismic distances.

Intermediate-depth earthquakes are peculiar events that are poorly understood compared to near-surface events. The high temperatures and pressures at these depths should make material ductile rather than brittle (e.g., Jeffreys 1924), i.e., earthquakes should not be occurring below 100-km depth. This cessation of earthquake occurrence has not been observed, and seismic events occur at depths close to 700 km. Many hypotheses have been proposed to explain the generation of these earthquakes, but there is no community-wide consensus. Difficulties in understanding intermediate-depth earthquakes also arise from insufficient constraints. Unlike shallow-focus earthquakes, these deeper events do not have surface expressions, and they often lack vigorous aftershock activity that helps identify the fault plane. For example, focal mechanism solutions of most intermediate-depth earthquakes have nodal planes that are nearly vertical and horizontal. In many cases, the ambiguity between the fault and the auxiliary plane remains, i.e., it is difficult to determine if the earthquake ruptured on a subhorizontal plane or a subvertical plane.

Back-projection analysis with a focus on obtaining depth information through phase combination can provide strong constraints on the depth dependence of the rupture (Kiser et al. 2011). As demonstrated in a previous section above, the combination of direct and depth-sensitive seismic

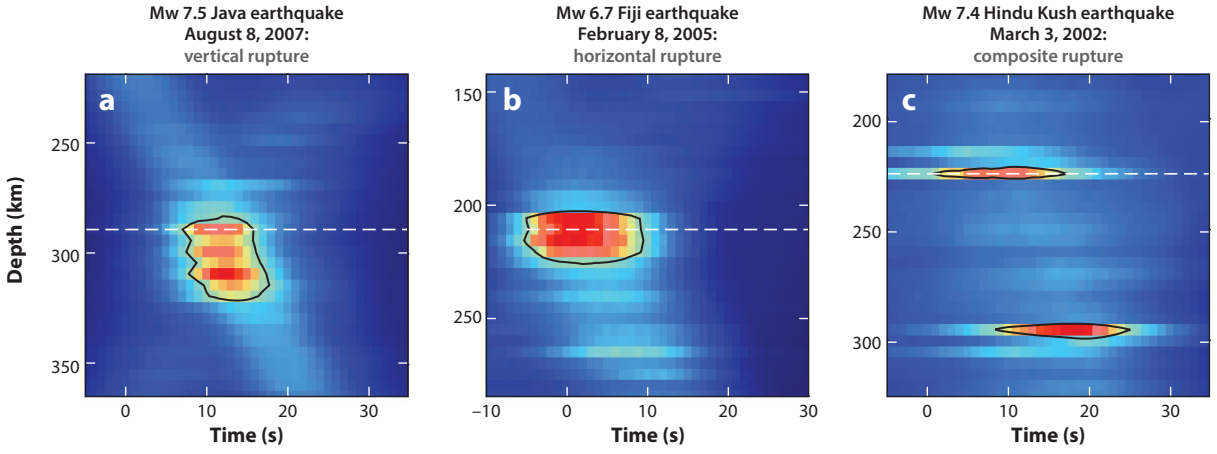

Figure 17

Comparison of rupture behavior as a function of depth and time for intermediate-depth earthquakes. The warmer colors indicate a higher amplitude, and the white dashed line shows the hypocentral depth. (*a*) An example of a vertical rupture observed for an Mw 7.5 earthquake in Java on August 8, 2007. (*b*) An example of a horizontal rupture observed for an Mw 6.7 earthquake in Fiji on February 8, 2005. (*c*) An example of a composite rupture observed for an Mw 7.4 earthquake in Hindu Kush on March 3, 2002.

phases results in depth resolution of the order of ±5 km. This spatial resolution limit is much smaller than the resolution in the lateral dimension using a single array at teleseismic distance. Placing emphasis on depth, ±5-km resolution implies that rupture propagation is observable for earthquakes as small as magnitude 6.5. To visualize the time evolution of rupture location in depth, the results are shown as a function of depth against time (**Figure 17**).

Analyses of 22 teleseismic, intermediate-depth earthquakes using data recorded by the Hi-net stations show two types of depth-dependence behavior (Kiser et al. 2011). Ruptures can propagate in depth, covering some vertical distance (**Figure 17*a***), or they can be confined in depth, propagating nearly horizontally (**Figure 17*b***). The events are not evenly distributed between these two types: Only 2 out of 22 events show propagation with a nearly continuous vertical extent. The rupture planes for intermediate-depth earthquakes, therefore, appear to be predominantly subhorizontal, a conclusion also reached by directivity analyses of intermediate-depth events (e.g., Warren et al. 2007). However, more than half of these events consist of multiple subhorizontal planes. The most spectacular example of these composite events was a magnitude 7.4 earthquake that occurred in the Hindu Kush region on March 03, 2002, at a hypocentral depth of 225 km (**Figure 17*c***). This earthquake shows two subhorizontal ruptures, one at about 175-km depth and another at about 250-km depth, i.e., they are separated in depth by about 75 km. The two episodes of energy release are also offset in time by about 10 s. If we assume that the two occurrences are related, then the depth and time separations indicate that the rupture that initiates must communicate with the location of the second event with a speed of about 7.5 km per second, well beyond the shear-wave speed at these depths. This observation advocates for dynamic triggering by the P wave generated by the initial rupture.

On the basis of the investigation of these earthquakes, intermediate-depth events are likely to have rupture on subhorizontal, not subvertical, nodal planes. These events are also perhaps more complex, involving multiple well-separated segments or different faults, than their shallow counterparts. These are valuable constraints in testing different hypotheses that attempt to explain why earthquakes occur at depths between 100 and 400 km (e.g., Frohlich 2006). For example, a

successful model must be able to account for the preferential occurrence of events on subhorizontal planes at different subduction zones. Models that can also reproduce the frequent occurrence of composite large (magnitude above 6.5) earthquakes are desirable (e.g., Kiser et al. 2011).

Event detection. Most back-projection studies thus far have focused on imaging rupture details of a specific earthquake. However, there is no limit on the time window over which the analysis can be performed, and array data can be continuously back-projected to the target source region. The continuous back-projection analysis constitutes a seismic event detection scheme that works particularly well immediately following a large mainshock or for better identification of relatively small earthquakes in areas where a local seismic network does not exist.

Vigorous aftershock activity following a large mainshock produces seismograms that are full of various body-wave and surface-wave arrivals (**Figure 18*a***). Identifying and characterizing individual aftershocks during this time period can be extremely challenging owing to difficulties in selecting the P and S wave arrivals that are typically used in event detection. The advantage of the back-projection analysis is the inherent slowness and azimuth filters. By seeking coherent energy that arrives with the slowness of a target phase (e.g., the direct P wave) and back-projecting to the source grid, unwanted seismic phases (e.g., reflections from the core–mantle boundary) are suppressed. Data can also be filtered to a relatively high frequency to reduce effects from large surface waves that can obscure body-wave arrivals. These features of the back-projection analysis naturally lead to a detection scheme of seismic sources.

As an example, consider the seismic activity following the Mw 9.0 Tohoku-oki, Japan, earthquake that occurred on March 11, 2011. Here, the objective is the detection of seismic sources rather than a detailed understanding of a particular event, and the time-dependent function that is stacked at the source should reflect this purpose. Linear stacks of normalized seismograms are often overwhelmed by large arrivals; hence a measure of waveform correlation between different stations at a given source grid location and time is more desirable. Furthermore, smaller earthquakes contain strong high-frequency energy, and data should be filtered accordingly. The selection of a specific frequency range should also be determined through inspection of the raw and stacked data. The higher the frequency of the signals, the more attenuated and scattered they become; therefore, there is an implicit high-frequency limit. This approach also imposes a limit on the smallest event that can be detected using a given set of array data at some specific distance from the source region.

The occurrence of seismic energy release within the target source region is often seen in the back-projected data as bursts of energy confined in time and space (**Figure 18*b*,*c***). The maximum back-projected value within the source region as a function of time (**Figure 18*b***) can be used for the initial detection scheme, and the back-projected map at the detection time (**Figure 18*c***) can be examined to identify the energy (i.e., if it is indeed a seismic source or some other feature) and its location. If multiple events are occurring at similar times, the back-projection method can find all events as long as they occur with spatial and temporal separation beyond the spatiotemporal resolution dictated by the data used (**Figure 18*d***).

When 25 hours of data following the 2011 Mw 9.0 Japan earthquake were analyzed, 600 events were confidently detected (Kiser & Ishii 2013). These events are distributed mostly in the mainshock rupture and surrounding area with a significant number in the outer-rise region (**Figure 19*a***). This distribution is considerably different from the local JMA catalog in which a strip of area along the trench on the landward side appears nearly aseismic with only a handful of events. In contrast, the global catalog by the USGS National Earthquake Information Center shows a similar distribution of events as detected by the back-projection method. Comparison of the

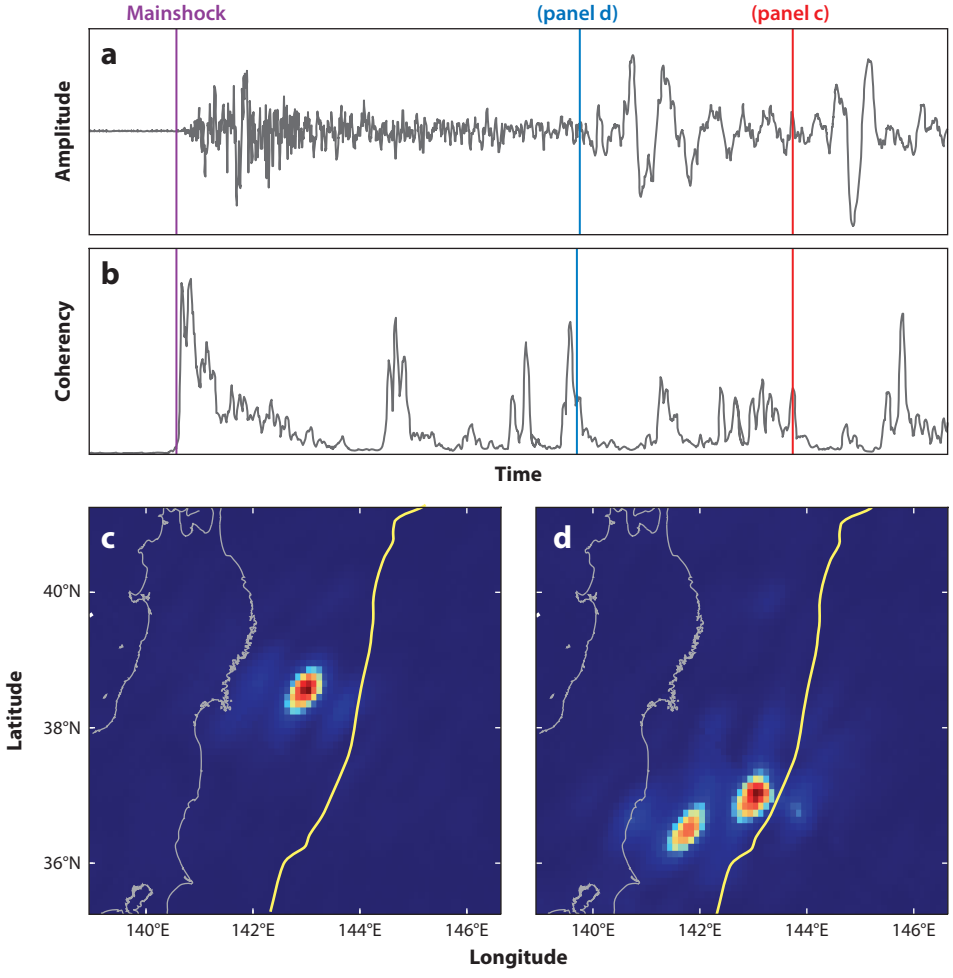

Figure 18

Aftershock detection using the back-projection method. (*a*) An example of a seismogram from station A25A of the Transportable Array in the United States between 05:55:50 and 06:16:52 UTC (1,262 s) on March 11, 2011. The purple vertical bar indicates the expected P arrival time from the mainshock. The red and blue bars are times corresponding to aftershocks shown in panels *c* and *d*, respectively. (*b*) Plot of the maximum coherence amplitude within the back-projected source region as a function of time; the purple vertical bar indicates the start of the March 11, 2011, mainshock. The time window corresponds to that shown in panel *a*. The peaks are associated with early aftershocks, which are not visible in panel *a*, demonstrating that array processing has successfully removed unwanted phase arrivals and emphasized event detection. (*c*) Map view of the back-projected coherency value at 06:01:24 UTC on March 11, 2011 (i.e., 906 s following the mainshock) corresponding to the red vertical bar in panels *a* and *b*. The thick yellow line is the trench location, and the thin gray curves are the coastlines. (*d*) Same as in panel *c* except that the time corresponds to the blue bar (05:56:07 UTC) in panels *a* and *b*. Two nearly simultaneous events can be detected. The event closer to the trench (37.05°N 143.04°E) occurs at 05:56:07 UTC, and the other event (36.65°N 141.94°E) happens 3 s later, at 05:56:10 UTC.

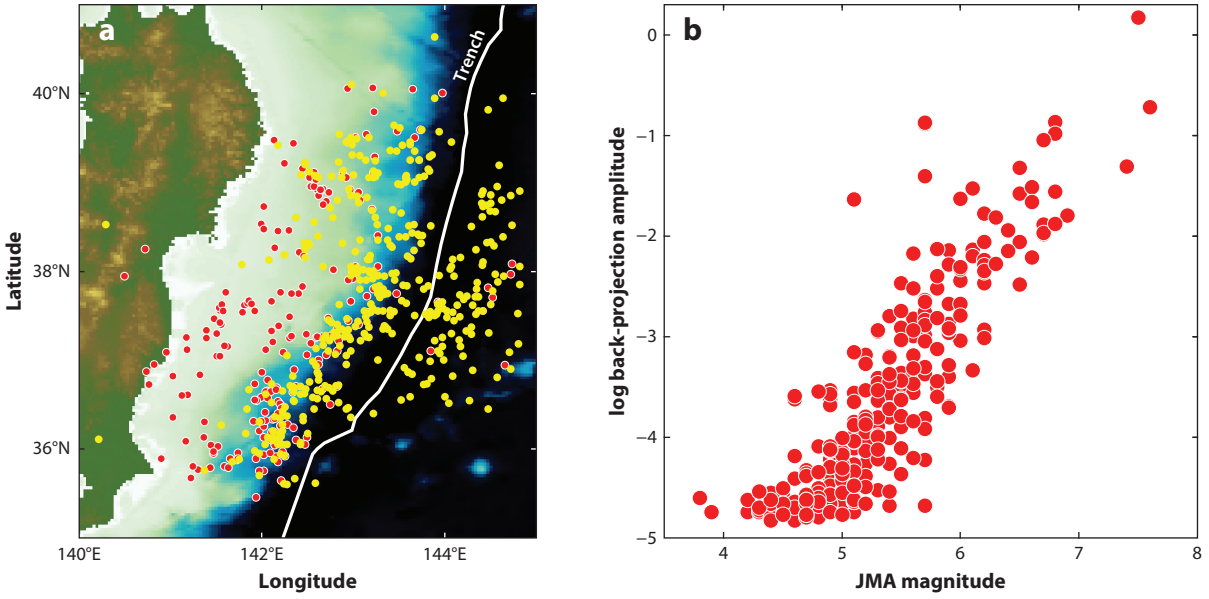

Figure 19

Events detected using the back-projection method during the first 25 h following the earthquake on March 11, 2011, Mw 9.0 Tohoku-oki, Japan. (*a*) Plot of the seismic event locations that have corresponding entries in the Japan Meteorological Agency (JMA) catalog (*red circles*) and those without (*yellow circles*). The background colors show topography (ETOPO2), and the white curve indicates the trench location. (*b*) Comparison of the back-projected amplitude using linear stacking and magnitudes given in the JMA catalog for events that exist in both catalogs.

back-projected catalog with the JMA catalog shows that events with magnitudes above 4.5 are mostly detectable using data from North America.

Even though the back-projection analysis cannot provide a magnitude estimate of a detected event, especially when a quantity such as coherence is considered, comparison with an existing catalog can produce an empirical relationship. For example, the amplitude of back-projected stacks, calculated using linear stacking of normalized traces, reflects relative amplitude variation with respect to a reference event. When this amplitude for detected events is compared with magnitudes given in the JMA catalog, a linear relationship between the logarithm of back-projected amplitude and JMA magnitude can be obtained (**Figure 19*b***). Such empirical relationships should be used with caution because effects such as differences in focal mechanism (hence initial amplitude leaving the source toward the array) are not included. Another quantity that is missing from the back-projection catalog is the event depth. For shallow events, such as those of the 2011 Japan sequence, the depth dimension is typically not included in the back-projection analysis; however, approaches such as those utilizing Green's functions from each source grid point to each station with direct and depth phases can lead to an improved depth estimate (Yagi et al. 2012).

The successful detection of seismic sources using the continuous back-projection analysis suggests that an automatic monitoring scheme can be implemented, similar to the global detection algorithm for glacial earthquakes based on surface waves (e.g., Ekström et al. 2003). The challenges are found in determining and setting discrimination threshold levels that can reliably identify events automatically. Examination of various parameters obtained through back-projection with an existing catalog should result in a set of criteria that could be used for such purposes.

FUTURE DIRECTIONS

With the occurrence of significant earthquakes, back-projection analysis continues to provide detailed images of rupture propagation. The emphasis is most likely to be shifted toward analyzing smaller earthquakes with smaller-aperture arrays that are located closer to the events (e.g., Allman & Shearer 2007) and that use regional and teleseismic phases (e.g., Roten et al. 2012). These data come with their own challenges such as complex arrivals associated with crustal structure, and techniques that combine the back-projection approach with numerical wavefield modeling become useful. There are advantages associated with shorter-distance, smaller arrays. They provide better azimuthal coverage, and hence smaller features are resolvable. The instruments are also easier to install logistically (compared with covering the entire Japanese islands or a north-to-south strip in the United States), and the spacing between stations could be reduced. For example, an exploration-style dense array covering a relatively small area with very high-frequency instruments can provide data for high-resolution, three-dimensional back-projection results (e.g., Brown et al. 2011). Such arrays can be set up around a highly active fault to determine the behavior of earthquakes occurring on different patches of the fault.

Combining the back-projection method with other techniques is a key to improving our understanding of earthquakes. For example, results from the back-projection analysis are mostly complementary to the finite-fault modeling approach, and integration of the two leads to better-constrained models of the earthquake process. This approach has already been employed by some groups (e.g., Lay et al. 2010a) and is producing promising results. For large earthquakes, differences in rupture behavior pose challenges for consolidation of the two methods, but these differences should become modest as the earthquake size decreases. The back-projection method may also evolve to process other types of observations or to investigate source parameters that are not possible with the current approach. For example, instead of waveforms from a given component, wavefield incidence using all three components could improve resolution. Relative amplitudes of waves recorded through the array may also be used to infer relative changes in focal mechanisms.

Another natural direction for back-projection analysis is to assimilate this method into general monitoring routines. Even at teleseismic distances, this method can provide a more thorough catalog of aftershock activities following large events. In addition, the method can be used to enhance continuous monitoring of regions where local stations are inadequate or where the global data set has difficulties identifying smaller events (e.g., ocean ridges in the southern hemisphere). In order for the back-projection method to be incorporated, several tasks must be performed. To begin, the method should be automated, as already implemented for the IRIS back-projection database. This long-term automation implies that permanent arrays or collections of permanent stations are necessary. If a limited number of seismic phases is used in the back-projection analysis (e.g., only the direct P waves), different source regions must be monitored by different networks. Furthermore, time correction information for each station must be set up for each region of interest prior to the analysis. This database can be constructed by processing the waves recorded by earthquakes from a given region, similar to the aftershocks used in Ishii et al. (2007).

Finally, application of the back-projection technique for studies of Earth's internal structure is also a possibility. Small scatterers are difficult to locate and characterize using conventional tomography or waveform analyses and are often studied in a statistical manner. Back-projection of relatively high-frequency data beyond the initial wave arrival can be used to identify scatterers or reflectors. For example, array data can be continuously scanned for significant scatterers around the array or around a target source region. In this case, recordings at different times (e.g., recordings from different earthquakes arriving from similar azimuths with respect to the array) can be used to enhance resolution (e.g., Korenaga 2013). This type of investigation starts to blur back-projection

analysis with techniques that already exist in the exploration community. After all, back-projection can be thought of as a type of data migration, and the merging of back-projection with other methods will lead to better ways of examining seismic sources and subsurface structure.

SUMMARY POINTS

1. The back-projection method time-reverses seismic array data to image the sources of coherent wavefronts in space and time.
2. The resolution of back-projection is determined by the aperture and density of stations within seismic arrays, as well as the slowness properties of the seismic phases utilized. Combining arrays or phases can significantly improve resolution.
3. Back-projection requires little a priori information to be applied, which facilitates the study of complex rupture properties including segmentation, multiple-fault triggering, and frequency dependence.

DISCLOSURE STATEMENT

M.I. is a member of the Board of Directors for Incorporated Research Institutions for Seismology (IRIS) and has received grant support from the US Geological Survey (USGS).

ACKNOWLEDGMENTS

We thank an anonymous reviewer for useful comments and Jocelyn Rice for assistance with drafting the manuscript. We also thank the IRIS Data Management Center for making Transportable Array data available and the National Research Institute for Earth Science and Disaster Prevention for making Hi-net data available.

LITERATURE CITED

Allman BP, Shearer PM. 2007. A high-frequency secondary event during the 2004 Parkfield earthquake. *Science* 318:1279–83

Avouac JP, Meng L, Wei S, Wang T, Ampuero JP. 2015. Lower edge of locked Main Himalayan Thrust unzipped by the 2015 Gorkha earthquake. *Nat. Geosci.* 8:708–11

Brown LB, Davenport K, Quiros DA, Han L, Chen C, et al. 2011. *Aftershock imaging with dense arrays (AIDA) following the August 23, 2011, Mw 5.8, Virginia Earthquake: Feasibility Demonstration and Preliminary Results*. Presented at AGU Fall Meet., Dec. 5–9, San Francisco, Abstr. S14B-06

Claerbout J. 1976. *Fundamentals of Geophysical Data Processing*. New York: McGraw-Hill

Darwin C. 1845. Chiloe and Concepcion: great earthquake. In *Journal of Researches into the Natural History and Geology of the Countries Visited During the Voyage of H.M.S. Beagle Round the World*, ed. J. Murray, pp. 301–12. London: Murray. 2nd ed.

Earle P, Shearer P. 1998. Observations of high-frequency scattered energy associated with the core phase PKKP. *Geophys. Res. Lett.* 25:405–8

Ekström G, Nettles M, Abers G. 2003. Glacial earthquakes. *Science* 302:622–24

Fan W, Shearer PM. 2015. Detailed rupture imaging of the 25 April 2015 Nepal earthquake using teleseismic *P* waves. *Geophys. Res. Lett.* 42:5744–52

Frohlich C. 2006. *Deep Earthquakes*. Cambridge, UK: Cambridge Univ. Press. 2nd ed.

Grandin R, Vallée M, Satriano C, Lacassin R, Klinger Y, et al. 2015. Rupture process of the $M_w = 7.9$ 2015 Gorkha earthquake (Nepal): insights into Himalayan megathrust segmentation. *Geophys. Res. Lett.* 42:8373–82

Hayes GP, Earle PS, Benz HM, Wald DJ, Briggs RW, USGS/NEIC Earthq. Response Team. 2011. 88 hours: the U.S. Geological Survey National Earthquake Information Center response to the 11 March 2011 M_w 9.0 Tohoku earthquake. *Seismol. Res. Lett.* 82:481–93

Hutko AR, Lay T, Garnero EJ, Revenaugh J. 2006. Seismic detection of folded, subducted lithosphere at the core-mantle boundary. *Nature* 441:333–36

Ishii M. 2011. High-frequency rupture properties of the M_w 9.0 off the Pacific coast of Tohoku earthquake. *Earth Planets Space* 63:609–14

Ishii M, Kiser E, Geist EL. 2013. Mw 8.6 Sumatran earthquake of 11 April 2012: rare seaward expression of oblique subduction. *Geology* 41:319–22

Ishii M, Shearer PM, Houston H, Vidale JE. 2005. Extent, duration and speed of the 2004 Sumatra–Andaman earthquake imaged by the Hi-net array. *Nature* 435:933–36

Ishii M, Shearer PM, Houston H, Vidale JE. 2007. Teleseismic *P* wave imaging of the 26 December 2004 Sumatra-Andaman and 28 March 2005 Sumatra earthquake ruptures using the Hi-net array. *J. Geophys. Res.* 112:B11307

Jeffreys H. 1924. *The Earth: Its Origin, History and Physical Constitution*. Cambridge, UK: Cambridge Univ. Press

Kaneshima S, Helffrich G. 1998. Detection of lower mantle scatterers northeast of the Marianna subduction zone using short-period array data. *J. Geophys. Res.* 103:4825–38

Kao H, Shan S-J. 2004. The source-scanning algorithm: mapping the distribution of seismic sources in time and space. *Geophys. J. Int.* 157:589–94

Kennett BLN, Engdahl ER. 1991. Traveltimes for global earthquake location and phase identification. *Geophys. J. Int.* 105:429–65

Kiser E, Ishii M. 2011. The 2010 Mw 8.8 Chile earthquake: triggering on multiple segments and frequency-dependent rupture behavior. *Geophys. Res. Lett.* 38:L07301

Kiser E, Ishii M. 2012a. Combining seismic arrays to image the high-frequency characteristics of large earthquakes. *Geophys. J. Int.* 188:1117–28

Kiser E, Ishii M. 2012b. The March 11, 2011 Tohoku-oki earthquake and cascading failure of the plate interface. *Geophys. Res. Lett.* 39:L00G25

Kiser E, Ishii M. 2013. Hidden aftershocks of the 2011 M_w 9.0 Tohoku, Japan earthquake imaged with the backprojection method. *J. Geophys. Res.* 118:5564–76

Kiser E, Ishii M, Langmuir CH, Shearer PM, Hirose H. 2011. Insights into the mechanism of intermediate-depth earthquakes from source properties as imaged by back projection of multiple seismic phases. *J. Geophys. Res.* 116:B06310

Kito T, Thomas C, Rietbrock A, Garnero E, Nippress SEJ, Heath AE. 2008. Seismic evidence for a sharp lithospheric base persisting to the lowermost mantle beneath the Caribbean. *Geophys. J. Int.* 174:1019–28

Koper KD, Hutko AR, Lay T, Ammon CJ, Kanamori H. 2011. Frequency-dependent rupture process of the 2011 Mw 9.0 Tohoku earthquake: comparison of short-period P wave backprojection images and broadband seismic rupture models. *Earth Planets Space* 63:599–602

Koper KD, Hutko AR, Lay T, Sufri O. 2012. Imaging short-period seismic radiation from the 27 February 2010 Chile (M_w 8.8) earthquake by back-projection of *P*, *PP*, and *PKIKP* waves. *J. Geophys. Res.* 117:B02308

Korenaga J. 2013. Stacking with dual bootstrap resampling. *Geophys. J. Int.* 195:2023–36

Larmat C, Montagner JP, Fink M, Capdeville Y, Tourin A, Clevede E. 2006. Time-reversal imaging of seismic sources and application to the great Sumatra earthquake. *Geophys. Res. Lett.* 33:L19312

Lay T, Ammon CJ, Hutko AR, Kanamori H. 2010a. Effects of kinematic constraints on teleseismic finite-source rupture inversion: Great Peruvian earthquakes of 23 June 2001 and 15 August 2007. *Bull. Seismol. Soc. Am.* 100:969–94

Lay T, Ammon CJ, Kanamori H, Koper KD, Sufri O, Hutko AR. 2010b. Teleseismic inversion for rupture process of the 27 February 2010 Chile (M_w 8.8) earthquake. *Geophys. Res. Lett.* 37:L13301

Lay T, Kanamori H, Ammon CJ, Hutko AR, Furlong K, Rivera L. 2009. The 2006–2007 Kuril Islands great earthquake sequence. *J. Geophys. Res.* 114:B11308

Lay T, Kanamori H, Ammon CJ, Koper KD, Hutko AR, et al. 2012. Depth-varying rupture properties of subduction zone megathrust faults. *J. Geophys. Res.* 117:B04311

Lay T, Kanamori H, Ammon CJ, Nettles M, Ward SN, et al. 2005. The great Sumatra-Andaman earthquake of 26 December 2004. *Science* 308:1127–33

McGuire JJ, Beroza GC. 2012. A rogue earthquake off Sumatra. *Science* 336:1118–19

McMechan GA, Luetgert JH, Mooney WD. 1985. Imaging of earthquake sources in Long Valley Caldera, California, 1983. *Bull. Seismol. Soc. Am.* 75:1005–20

Meng L, Ampuero J-P, Bürgmann R. 2014. The 2013 Okhotsk deep-focus earthquake: rupture beyond the metastable olivine wedge and thermally controlled rise time near the edge of a slab. *Geophys. Res. Lett.* 41:3779–85

Meng L, Ampuero J-P, Stock J, Duputel Z, Luo Y, Tsai VC. 2012. Earthquake in a maze: compressional rupture branching during the 2012 M_w 8.6 Sumatra earthquake. *Science* 337:724–26

Meng L, Inbal A, Ampuero J-P. 2011. A window into the complexity of the dynamic rupture of the 2011 Mw 9 Tohoku-Oki earthquake. *Geophys. Res. Lett.* 38:L00G07

Meng L, Zhang A, Yagi Y. 2016. Improving back projection imaging with a novel physics-based aftershock calibration approach: a case study of the 2015 Gorkha earthquake. *Geophys. Res. Lett.* 43:628–36

Ni S, Kanamori H, Helmberger D. 2005. Seismology: energy radiation from the Sumatra earthquake. *Nature* 434:582

NOAA (Natl. Ocean. Atmos. Adm.), Natl. Geophys. Data Cent., US Dep. Commer. 2006. *2-minute gridded global relief data (ETOPO2v2)*. June, Natl. Cent. Environ. Inf. (NCEI), Boulder, CO. **http://www.ngdc.noaa.gov/mgg/fliers/06mgg01.html**

Obara K, Kasahara K, Hori S, Okada Y. 2005. A densely distributed high-sensitivity seismograph network in Japan: Hi-net by National Research Institute for Earth Science and Disaster Prevention. *Rev. Sci. Instrum.* 76:021301

Okada Y, Kasahara K, Hori S, Obara K, Sekiguchi S, et al. 2004. Recent progress of seismic observation networks in Japan: Hi-net, F-net, K-NET and KiK-net. *Earth Planets Space* 56:xv–xxviii

Park J, Song T-RA, Tromp J, Okal E, Stein S, et al. 2005. Earth's free oscillations excited by the 26 December 2004 Sumatra-Andaman earthquake. *Science* 308:1139–44

Rietbrock A, Scherbaum F. 1994. Acoustic imaging of earthquake sources from Chalfant Valley, 1985, aftershock series. *Geophys. J. Int.* 119:260–68

Rost S, Thomas C. 2002. Array seismology: methods and applications. *Rev. Geophys.* 40:1008

Roten D, Miyake H, Koketsu K. 2012. A Rayleigh wave back-projection method applied to the 2011 Tohoku earthquake. *Geophys. Res. Lett.* 39:L02302

Schimmel M, Paulssen H. 1997. Noise reduction and detection of weak, coherent signals through phase weighted stacks. *Geophys. J. Int.* 130:497–505

Spudich P, Cranswick E. 1984. Direct observation of rupture propagation during the 1979 Imperial Valley earthquake using a short baseline accelerometer array. *Bull. Seismol. Soc. Am.* 74:2083–114

Spudich P, Frazer LN. 1984. Use of ray theory to calculate high-frequency radiation from earthquake sources having spatially variable velocity and stress drop. *Bull. Seismol. Soc. Am.* 74:2061–82

Titov V, Rabinovich AB, Mofjeld HO, Thomson RE, González FI. 2005. The global reach of the 26 December 2004 Sumatra tsunami. *Science* 309:2045–48

Trabant C, Hutko AR, Bahavar M, Karstens R, Ahern T, Aster R. 2012. Data products at the IRIS DMC: Stepping-stones for research and other applications. *Seismol. Res. Lett.* 83:846–54

Wang D, Mori J. 2011. Frequency-dependent energy radiation and fault coupling for the 2010 Mw8.8 Maule, Chile, and 2011 Mw9.0 Tohoku, Japan, earthquakes. *Geophys. Res. Lett.* 38:L22308

Wang D, Mori J, Uchide T. 2012. Supershear rupture on multiple faults for the M_w 8.6 off northern Sumatra, Indonesia earthquake of April 11, 2012. *Geophys. Res. Lett.* 39:L21307

Warren LM, Hughes AN, Silver PG. 2007. Earthquake mechanics and deformation in the Tonga-Kermadec subduction zone from fault plane orientations of intermediate- and deep-focus earthquakes. *J. Geophys. Res.* 112:B05314

Wessel P, Smith WHF. 1995. New version of the Generic Mapping Tools released. *Eos Trans. AGU* 76:F329

Yagi Y, Nakao A, Kasahara A. 2012. Smooth and rapid slip near the Japan Trench during the 2011 Tohoku-oki earthquake revealed by a hybrid back-projection method. *Earth. Planet. Sci. Lett.* 355:94–101

Yagi Y, Okuwaki R. 2015. Integrated seismic source model of the 2015 Gorkha, Nepal, earthquake. *Geophys. Res. Lett.* 42:6229–35

Yao H, Gerstoft P, Shearer PM. 2011. Compressive sensing of the Tohoku-Oki Mw 9.0 earthquake: frequency dependent rupture modes. *Geophys. Res. Lett.* 38:L20310

Yao H, Shearer PM, Gerstoft P. 2012. Subevent location and rupture imaging using iterative backprojection for the 2011 Tohoku M_w 9.0 earthquake. *Geophys. J. Int.* 190:1152–68

Ye L, Lay T, Kanamori H, Koper KD. 2013. Energy release of the 2013 M_w 8.3 Sea of Okhotsk earthquake and deep slab stress heterogeneity. *Science* 341:1380–84

Yue H, Lay T, Koper KD. 2012. *En échelon* and orthogonal fault ruptures of the 11 April 2012 great intraplate earthquakes. *Nature* 490:245–49

Annual Review
of Earth and
Planetary Sciences
Volume 45, 2017

Contents

Errata

An online log of corrections to *Annual Review of Earth and Planetary Sciences* articles may be found at http://www.annualreviews.org/errata/earth